Contributions to Mineralogy and Petrology (2018) 173:103
https://doi.org/10.1007/s00410-018-1533-7

ORIGINAL PAPER

Ti K-edge XANES study on the coordination number and oxidation state of Titanium in pyroxene, olivine, armalcolite, ilmenite, and silicate glass during mare basalt petrogenesis

F. P. Leitzke[1] · R. O. C. Fonseca[1,2] · J. Göttlicher[3] · R. Steininger[3] · S. Jahn[2] · C. Prescher[2] · M. Lagos[1]

Received: 1 June 2018 / Accepted: 12 November 2018 / Published online: 20 November 2018

Abstract

Lunar mare basalts are a product of partial melting of the lunar mantle under more reducing conditions when compared to those expected for the Earth's upper mantle. Alongside Fe, Ti can be a major redox sensitive element in lunar magmas, and it can be enriched by up to a factor of ten in lunar basaltic glasses when compared to their terrestrial counterparts. Therefore, to better constrain the oxidation state of Ti and its coordination chemistry during lunar magmatic processes, we report new X-ray absorption near edge structure (XANES) spectroscopy measurements for a wide range of minerals (pyroxene, olivine, Fe–Ti oxides) and basaltic melt compositions involved in partial melting of the lunar mantle. Experiments were conducted in 1 bar gas-mixing furnaces at temperatures between 1100 and 1300 °C and oxygen fugacities (fO_2) that ranged from air to two orders of magnitude below the Fe–FeO redox equilibrium. Run products were analysed via electron microprobe and XANES Ti K-edge. Typical run products had large (> 100 µm) crystals in equilibrium with quenched silicate glass. Ti K-edge XANES spectra show a clear shift in energy of the absorption edge features from oxidizing to reducing conditions and yield an average valence for Fe–Ti oxides (armalcolite and ilmenite) of 3.6, i.e., a 40% of the overall Ti is Ti^{3+} under fO_2 conditions relevant to lunar magmatism (IW − 1.5 to − 1.8). Pyroxenes and olivine have average Ti valence of 3.75 (i.e., 25% of the overall Ti is trivalent), while in silicate glasses Ti is exclusively tetravalent. Pre-edge peak intensities also indicate that the coordination number of Ti varies from an average V-fold in silicate glass to VI-fold in the Fe–Ti oxides and a mixture between IV and VI-fold coordination in the pyroxenes and olivine, with up to 82% $^{[IV]}Ti^{4+}$ in the pyroxene. In addition, our results can help to better constrain the $Ti^{3+}/\sum Ti$ of the lunar mantle phases during magmatic processes and are applied to provide first insights into the mechanisms that may control Ti mass-dependent equilibrium isotope fractionation in lunar mare basalts.

Keywords Mantle · Experimental petrology · XANES · Mare basalts · Moon

Introduction

Lunar petrogenesis has occurred at oxygen fugacity (fO_2) conditions below the Fe–FeO (Iron-Wüstite–IW–Myers and Eugster 1983) redox buffer (e.g., Papike et al. 2005; Nicholis and Rutherford 2009), which is over three orders of magnitude more reduced than the average terrestrial upper mantle (cf., Ballhaus 1993; Frost and McCammon 2008). The clear Eu anomaly observed in lunar basalts, which is caused by the preferential partitioning of Eu^{2+} into the plagioclase (Brophy and Basu 1990; O'Hara and Niu 2015), as well as the presence of metallic Fe, troilite (FeS), and armalcolite [$(Mg,Fe)Ti_2O_5$], which hosts reduced Ti^{3+} in its structure (cf., Kesson and Lindsley 1975; Stanin and Taylor 1980) are among the direct evidence for the reduced nature of the lunar mantle. Direct measurements of the intrinsic fO_2 as

Communicated by Jochen Hoefs.

✉ F. P. Leitzke
felipe.leitzke@uni-bonn.de

[1] Steinmann-Institut für Geologie, Mineralogie und Paläontologie, Rheinische Friedrich-Wilhelms-Universität Bonn, Poppelsdorfer Schloss (Mineralogisches Museum), 53115 Bonn, Germany

[2] Institut für Geologie und Mineralogie, Universität zu Köln, 50674 Cologne, Germany

[3] Institute for Photon Science and Synchrotron Radiation, Karlsruhe Institute für Technologie, 76021 Karlsruhe, Germany

recorded by lunar samples using solid-electrolyte cells, and use of V valence oxybarometery through X-ray absorption spectroscopy, have confirmed that lunar basaltic magmatism takes place below the IW buffer (Sato et al. 1973; Karner et al. 2006). The mechanism of reduction of lunar magmas has been considered to be the reaction between reduced carbon and lunar magmas, as evidenced by the observation that carbon monoxide is the most abundant gas released during lunar volcanism, followed by loss of sulfur (Moore et al. 1972; DesMarais et al. 1972; Sato 1976). Lunar basalts show a larger range of TiO_2 contents when compared to their terrestrial counterparts (Meyer 2012). Lunar basaltic glasses can reach TiO_2 concentrations as high as 16 wt% (Marvin and Walker 1978), and are considered to be products of partial melting of the lunar mantle mafic cumulates after the solidification of a magma ocean (e.g., Ringwood and Kesson 1976; Beard et al. 1998). High-Ti mare basalts are thought to result from melting at more reducing conditions (IW-2) than those prevalent throughout the petrogenesis of low-Ti basalts (~IW) (Karner et al. 2006; Fonseca et al. 2014; Leitzke et al. 2016). This assertion is supported by the fact that olivines in high-Ti basalts are more depleted in siderophile elements like Ni and Cr than low-Ti basalts at similar Mg# (Karner et al. 2003). Even though the TiO_2–Ti_2O_3 redox buffer is located at more reduced conditions than IW, the idea that Ti^{3+} cannot coexist with high FeO contents due to redox exchanges during cooling has been refuted by direct measurements in refractory inclusions found in meteorites, which yielded a $Ti^{3+}/\sum Ti$ ratio from 0.37 to 0.79 (Simon et al. 2007), as well as by the discovery of Tistarite (Ti_2O_3) and Grossmanite ($CaTi^{3+}AlSiO_6$) in the Allende meteorite (Ma and Rossmann 2009a, b). Regarding lunar magmatism, there have been a number of studies dealing with X-ray absorption near edge structure (XANES) spectroscopy to determine speciation of Ti in lunar phases, with recent works in lunar pyroxene and olivine from both experimental and natural samples showing either significant (Krawczynski et al. 2010) or negligible (Simon et al. 2014) Ti^{3+}, depending on the petrological history of the samples, and their mineral and mantle source composition (Simon and Sutton 2017, 2018).

Titanium K-edge XANES data on lunar minerals and basaltic glass proxies equilibrated under controlled temperature, melt composition and fO_2 provide the basis for understanding the coordination number of Ti and its oxidation state in the lunar mantle, and therefore, the resolvable differences in the Ti isotope composition of terrestrial and lunar samples (Millet et al. 2016). Here we present the results of an experimental micro-XANES investigation on the redox state and coordination environment of Ti on synthetic lunar minerals and basaltic glasses over a wide range of compositions and fO_2 conditions relevant to lunar magmatic processes. Our results offer a broader dataset of XANES Ti K-edge measurements applicable to lunar petrology and estimates of the $Ti^{3+}/\sum Ti$ of lunar minerals and mantle melts. In addition, we also report insights from ab initio calculations into the mechanisms that can control Ti mass-dependent equilibrium isotope fractionation in the lunar mantle context.

Materials and methods

Starting compositions and experimental methods

Starting compositions were chosen based on the CMAS (CaO–MgO–Al_2O_3–SiO_2) + TiO_2 system, and have been described in detail by several experimental studies (e.g., Longhi 1987; Mallmann and O'Neill 2009; Fonseca et al. 2014; Leitzke et al. 2016). The "base" mix was modified by adding 1–20 wt% TiO_2 to produce low to high-Ti lunar basalts analogues (Table 1). The absence of FeO in some of the compositions was to avoid any potential interaction between FeO and TiO_2 during quenching (Borisov et al. 2013). The proportion SiO_2/TiO_2 for the compositions with 5, 10 and 20 wt% TiO_2 was established in relation to the binary anorthite–diopside as described in O'Neill et al. (2008), while the ratio between other major elements and

Table 1 Major element compositions (cg/g) of starting materials

Starting mix	CaO	MgO	Al_2O_3	SiO_2	TiO_2	Cr_2O_3	FeO	Total
T1-10	16.42	23.62	4.70	43.90	10.02	–	–	98.66
T1-20	14.65	21.06	4.20	39.16	19.80	–	–	98.87
T5-20	7.70	22.96	5.41	41.74	21.67	–	–	99.48
T7-5	17.15	24.68	4.97	46.06	5.07	1.41	–	99.34
T7-10	16.27	23.40	4.68	43.47	9.99	1.35	–	99.16
T7-20	14.53	16.90	4.16	43.84	19.61	1.20	–	100.24
T8-20	10.50	16.10	19.17	36.00	18.10	–	–	99.87
FT1	17.91	8.43	5.13	47.87	1.03	0.47	17.83	98.67
FT1-5	17.29	8.14	4.95	46.22	5.06	0.44	17.19	99.29
FT1-10	16.42	7.73	4.70	43.90	10.02	0.42	16.32	99.51
FT1-20	14.65	6.89	4.19	39.16	19.73	0.38	14.58	99.58

SiO_2 remained constant. At one-atmosphere, these compositions are known to crystallize large (> 100 µm) and euhedral armalcolite, ilmenite, pyroxene, and olivine in equilibrium with high-TiO_2 (2–20 wt%) silicate melt (see Leitzke et al. 2016). High-purity oxide powders (SiO_2, MgO, Al_2O_3, and TiO_2) were ground with $CaCO_3$ under acetone using an agate mortar. Additionally, Fe_2O_3 (base mix FT1), and Cr_2O_3 (base mix T7), were also added to the starting mixes to assess if a redox exchange could have occurred during quenching, as well as to have mineral compositions, which more closely represent natural conditions. Mixes were subsequently dried, pressed into pellets and placed in a quartz crucible inside a furnace to decarbonate overnight at 900 °C. Experiments (see Table 1) were conducted in vertical gas-mixing tube furnaces using the wire loop technique (Donaldson et al. 1975). This method uses loops of a refractory metal wire (Pt-Rh or Re in this study), on which a slurry made from a mixture between the sample powders, H_2O and polyethylene glycol is suspended. The metal loops plus sample slurry are then hung inside a one-atmosphere vertical tube furnace at temperatures around 50 to 100 °C above the liquidus of each composition and under the redox conditions of interest. Oxygen fugacity was imposed by mixing CO-CO_2 in different proportions using Mykrolis mass flow controllers. The CO-CO_2 proportions required to obtain equilibrium gas species at the desired fO_2 were calculated using an Excel macro as described in Kress et al. (2004) and double-checked using an internal CaO–Y_2O_3-stabilized ZrO_2 electrolyte cell. Measured fO_2 values were within 0.5 log-bar units of the calculated values. Temperature was monitored using an internal type B ($Pt_{70}Rh_{30}$–$Pt_{94}Rh_6$) thermocouple. Experiments with Fe-bearing starting mixes were performed with Re-wire to avoid Fe-loss to the metal wire (e.g., Pt). In this case, temperature was set to 800 °C with the gas mixture already flowing through the furnace tube, before the wire loop with the sample placed into the furnace. This step was necessary to avoid oxidation and volatilization of the Re-wire. The temperature was then raised to supra-liquidus conditions and kept there for 3 h to ensure that the powders were completely molten and homogenized. Cooling ramps were chosen to maximize crystal growth (at least 100 µm) for XANES analysis and the temperature was lowered to the nominal value of the experiment, where it remained for 48 to 96 h to ensure equilibrium was reached. Quenching of the samples was carried out in air by removing the sample holder from the top of the furnace or dropping it into a beaker filled with water. Quenched samples were recovered, mounted in epoxy resin and polished for chemical analysis. A summary of experimental run conditions is shown in Table 2.

Electron microprobe analysis

Analysis of major and minor elements (CaO, MgO, Al_2O_3, SiO_2, TiO_2, Cr_2O_3 and FeO) was carried out using a JEOL JXA 8900 electron probe micro-analyser (EPMA). Measurements were carried out in Wavelength Dispersive mode (WDS), employing 15 kV accelerating voltage, 15 nA beam current. Crystals and glasses were measured with an electron beam defocused to 5 µm. Peak to background calibrations were performed on a basaltic glass from the Juan de Fuca ridge (VG2), as well as on rutile, San Carlos olivine, and chromite. Differences in the electron absorption properties between standards and the experimental phases were

Table 2 Summary of run conditions for each experiment at 1 bar vertical tube gas-mixing furnaces

Starting materials	log fO_2	Δ IW	Cooling ramp (°/min)	Target temp. (°C)	Duration (h)	Run products[a]	CO:CO_2 (SCCM)[b]
FT1-10; FT1-20	− 15.1	− 1.8	0.04	1100	72	cpx + ilm + glass; cpx + ttn + arm + glass	90:4
FT1; FT1-5	− 13.7	− 1.5	0.04	1200	60	cpx + glass	110:4
T7-5, T7-10	− 13.2	− 1.9	0.04	1250	96	cpx + glass; cpx + ol + glass	200:5
T1-20, T5-20, T8-20	− 12.9	− 1.7	0.03	1260	48	arm + ol + glass; opx + arm + glass; arm + glass	120:4
T1-10	− 12.7	− 1.7	0.05	1280	72	ol + glass	140:4
T1-10, FT1-10, T7-20	− 0.7	10.0	–	1300	24	glass	Air[c]
T1-10, FT1-10, T7-20	− 12.9	− 2.1	–	1300	24	glass	160:5
T5-20	− 0.7	10.0	0.03	1260	96	opx + arm + glass	Air[c]
T5-20	− 7.8	3.4	0.04	1260	96	opx + arm + glass	15:300

cpx clinopyroxene, *glass* silicate glass, *ilm* ilmenite, *arm* armalcolite, *ol* olivine, *opx* orthopyroxene, *ttn* titanite

[a]Mineral assemblages in each experiment are separated by ";" relatively to column "Starting Materials"

[b]Proportion between CO:CO_2 mixed in the mass flow controllers in Standard Cubic Centimeter per Minute (SCCM), which was set to define a specific value of fO_2 during the experiment

[c]Top and bottom of the furnace were not sealed, allowing air to flow, i.e., an oxidizing atmosphere

corrected via the ZAF algorithm. Values presented for this study consist of averages of five to ten measurements carried out on each phase.

XANES spectroscopy

Currently, micro-XANES is one of the most appropriate element specific techniques to study the chemical element spatial coordination, bond strength and oxidation state in geochemistry and cosmochemistry (e.g., Simon et al. 2007, 2016; Dyl et al. 2011; Righter et al. 2011, 2016; Sutton et al. 2017). However, there are still scarce data of extra-terrestrial materials analysed through XANES (Farges and Wilke 2015), with just a few Ti K-edge absorption studies applied to lunar petrology, a subject of research that has gained importance in the last decade (e.g., Krawzcinski et al. 2009; Simon et al. 2014; Simon and Sutton 2017, 2018). XANES analysis consists of measuring the photon energy spectrum resulting from focusing an X-ray beam to excite a 1s electron to a higher energy unoccupied p-state (Berry and O'Neill 2004). When the primary beam exceeds the binding energy of the 1s shell electron of the atom, the absorption spectrum is stepwise increased, which is called "K-edge". In addition a peak like higher absorption occurs for primary energies close to the binding energy, namely the "white line" (Joly and Grenier 2016). Moreover, pre- and post-edge features of the spectra, included at the Extended X-ray absorption fine structure (EXAFS) region, can be attributed to the similarity of the energies of bound electronic states to free ion levels, and are used to identify bonding distances and site geometry on minerals and silicate melts (e.g., Waychunas 1987; Berry and O'Neill 2004).

Titanium K-edge XANES spectra were acquired using a Si (111) double crystal monochromator at the SUL-X beamline of the ANKA synchrotron facility (Karlsruhe, Germany). The X-ray beam was focused to 50×50 μm^2 at sample position with a KB mirror system on each phase (glass and crystals). Measurements had to be performed in fluorescence mode due to the thickness of the polished sections. To reduce self-absorption effects that occur at high-Ti concentrations in fluorescence mode, the sample surface was aligned 85° towards the beam (close to perpendicular position) and the sample surface–detector angle resulted then in 5° (close to grazing exit conditions). The sample chamber was kept under vacuum to avoid absorption of low energy X-rays under air. Energy shifts were monitored by measuring a Ti metal foil every five sample measurements and aligned to the first maximum of the first derivative of the spectrum at 4966 eV. Because crystal orientation can be a source of uncertainty (e.g., Simon et al. 2007), we measured more than one crystal in the same experiment, in similar fashion to what was described by Sutton et al. (2017) but no attempt was done to correct for this issue. XANES data were processed with the Athena programme of the IFEFFIT software package, with pre-edge peaks fitted using non-linear least square best fits to the line shapes (Ravel and Newville 2005).

Results

Run products and major element composition

Typical run products had large (> 100 μm) euhedral to subhedral crystals (diopside, augite, enstatite, forsterite, armalcolite and ilmenite) in chemical equilibrium with quenched silicate glass (Fig. 1). The modal proportion between crystals and silicate glass was calculated using the software ImageJ® histogram feature, which counts the frequency of the different levels of gray on back-scattered electron images of polished thick sections. By applying this method, a representative average proportion of crystals and silicate glass is approximately 0.3:0.7, respectively. Electron microprobe major element compositions are given in Table 3 and Ti total contents are reported as TiO_2. Because some of the

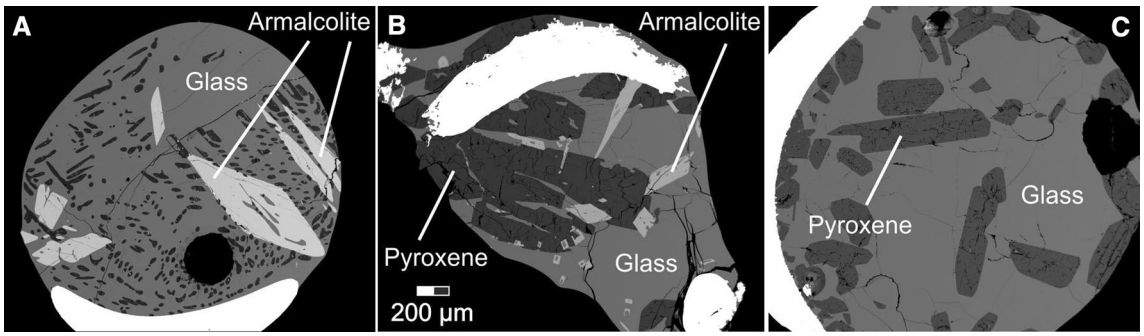

Fig. 1 Back-scattered electron images of typical experimental run products: **a** large euhedral to subhedral armalcolite crystals in equilibrium with silicate glass (T1-20, 1260 °C, ΔIW-1.7); **b** euhedral orthopyroxene (enstatite) crystals in equilibrium with armalcolite and silicate glass (T5-20, 1260 °C, ΔIW-1.7); **c** euhedral clinopyroxene (diopside) crystals in chemical equilibrium with silicate glass (T7-5, 1250 °C, ΔIW-1.9)

Table 3 WDS-EPMA major and minor elements average concentration and uncertainty ($n = 5$/each phase)

Experiment	Temp. (°C)	ΔIW	Phase	MgO	±	FeO_T	±	TiO_{2T}	±	SiO_2	±	Al_2O_3	±	CaO	±	Cr_2O_3	±	Σ
FT1-10	1100	− 1.8	Cpx	13.4	0.6	9.0	1.0	2.9	0.3	50.2	0.6	1.7	0.2	21.2	0.2	1.1	0.1	99.5
			Ilm	4.5	0.1	36.6	0.5	57.5	0.4	0.08	0.02	0.17	0.02	0.23	0.03	2.1	0.1	101.2
			Glass	3.6	0.1	17.0	0.2	12.5	0.3	44.6	1.2	6.5	0.1	14.3	0.1	0.2	0.1	98.7
FT1-20	1100	− 1.8	Cpx	15.7	0.4	11.9	0.6	2.9	0.1	51.6	1.9	1.3	0.1	18.8	0.6	0.2	0.1	102.3
			Ttn	0.22	0.03	0.7	0.1	40.4	0.7	29.0	0.6	0.38	0.04	27.9	0.2	0.3	0.1	98.9
			Arm	6.3	0.3	17.5	0.4	76.4	0.9	0.2	0.1	0.71	0.04	0.10	0.03	0.8	0.1	102.0
			Glass	4.3	0.4	17.8	1.2	12.6	2.1	45.0	0.6	6.7	0.5	13.7	0.9	0.2	0.1	100.3
FT1	1200	− 1.5	Cpx	12.6	0.1	11.7	0.4	0.5	0.1	49.9	1.2	1.6	0.2	21.5	0.1	1.0	0.1	98.7
			Glass	4.2	0.0	24.2	0.3	1.5	0.1	46.7	0.5	7.5	0.1	15.6	0.1	0.3	0.1	100.0
FT1-5	1200	− 1.5	Cpx	14.4	0.2	8.0	0.1	1.6	0.1	49.9	1.1	1.5	0.1	21.9	0.2	1.5	0.1	98.9
			Glass	4.7	0.1	19.5	0.3	7.1	0.1	46.8	0.3	6.7	0.1	15.5	0.1	0.3	0.1	100.6
FT1-10	1300	10.0	Glass	5.9	0.1	19.3	0.2	9.4	0.2	42.2	0.5	5.2	0.1	17.5	0.1	0.4	0.2	99.9
FT1-10	1300	− 2.1	Glass	7.3	0.1	4.6	0.1	11.5	0.3	50.0	2.0	6.8	0.1	19.8	0.4	0.5	0.1	100.5
T1-10	1280	− 1.7	Ol	57.7	0.3	bdl	–	0.09	0.03	42.5	1.0	bdl	–	0.34	0.01	bdl	–	100.8
			Glass	14.1	0.1	bdl	–	11.6	0.2	48.9	1.6	6.3	0.3	19.5	0.2	bdl	–	100.4
T1-10	1300	10.0	Glass	16.3	0.1	bdl	–	12.6	0.1	46.0	1.3	5.3	0.1	19.5	0.2	bdl	–	99.7
T1-10	1300	− 2.1	Glass	16.1	0.5	bdl	–	12.7	0.2	45.0	0.7	6.2	0.1	21.1	0.1	bdl	–	101.0
T1-20	1260	− 1.7	Ol	56.8	0.2	bdl	–	0.14	0.03	43.2	0.4	bdl	–	0.24	0.03	bdl	–	100.4
			Arm	15.3	0.1	bdl	–	88.1	0.3	0.09	0.02	1.1	0.1	0.2	0.1	bdl	–	104.8
			Glass	13.6	0.2	bdl	–	15.4	0.2	47.4	0.9	5.9	0.1	16.8	0.2	bdl	–	99.1
T5-20	1260	− 1.7	Opx	39.7	0.2	bdl	–	1.4	0.2	56.6	1.3	0.5	0.1	0.36	0.02	bdl	–	98.5
			Arm	14.4	0.2	bdl	–	88.0	0.6	0.10	0.02	1.5	0.1	0.03	0.02	bdl	–	104.0
			Glass	11.8	0.1	bdl	–	12.3	0.3	51.2	0.6	9.9	0.1	14.8	0.1	bdl	–	100.0
T5-20	1260	10.0	Opx	38.4	0.3	bdl	–	1.1	0.1	59.5	0.4	0.32	0.04	0.3	0.1	bdl	–	99.5
			Arm	18.6	0.2	bdl	–	78.5	0.6	0.23	0.03	2.1	0.1	0.21	0.03	bdl	–	99.7
			Glass	12.2	0.1	bdl	–	16.7	0.2	50.8	0.2	8.7	0.1	10.9	0.1	bdl	–	99.3
T5-20	1260	3.4	Opx	38.6	0.2	bdl	–	1.1	0.3	60.4	0.2	0.3	0.1	0.41	0.04	bdl	–	100.8
			Arm	19.1	0.1	bdl	–	78.1	0.6	0.28	0.01	2.0	0.1	0.05	0.02	bdl	–	99.5
			Glass	13.7	0.1	bdl	–	16.6	0.2	50.8	0.2	8.2	0.1	10.4	0.1	bdl	–	99.7
T7-5	1250	− 1.9	Cpx	19.9	0.2	bdl	–	2.0	0.3	53.7	0.4	1.7	0.1	21.2	0.4	1.4	0.1	99.8
			Glass	14.0	0.0	bdl	–	10.5	0.1	48.9	0.2	9.8	0.1	16.7	0.1	0.8	0.1	100.6
T7-10	1250	− 1.9	Cpx	20.8	0.5	bdl	–	2.6	0.6	54.3	0.8	1.1	0.2	21.4	0.1	0.3	0.1	100.3
			Ol	53.7	2.8	bdl	–	0.14	0.05	43.6	1.1	0.2	0.1	0.52	0.01	1.0	0.1	99.1
			Glass	14.0	0.2	bdl	–	10.9	0.1	49.7	0.3	9.3	0.1	15.8	0.1	0.18	0.03	100.1
T7-20	1300	10.0	Glass	16.3	0.2	bdl	–	20.0	0.2	43.2	1.0	4.6	0.1	14.5	0.1	1.0	0.2	99.6
T7-20	1300	− 2.1	Glass	17.2	0.2	bdl	–	21.8	0.1	42.8	0.7	4.3	0.2	13.1	0.1	1.2	0.3	100.4
T8-20	1260	− 1.7	Arm	13.5	0.2	bdl	–	82.5	0.9	0.12	0.03	7.9	0.2	0.11	0.02	bdl	–	104.1
			Glass	13.4	0.1	bdl	–	7.9	0.1	46.3	0.7	21.2	0.1	11.4	0.1	bdl	–	100.2

bdl below detection limit (< 0.01 wt%), starting compositions did not contain these elements

phases had substantial amounts of Ti^{3+}, the number of oxygens was overestimated, resulting in sum values greater than 100 wt%. Crystal size was controlled by the cooling rate of each experiment and the TiO_2 content of the silicate melt, which proved to have a depolymerizing effect (see Leitzke et al. 2016). Among the silicates, diopside and augite crystals display the highest TiO_2 contents ranging from 0.5 to 2.9 wt% or 0.01 to 0.09 atoms per formula unit (apfu), which is not high enough to accurately determine $Ti^{3+}/\sum Ti$ using concentrations measured by electron microprobe (see Simon et al. 2007). The $^{[IV]}Al$ of cpx did not exceed 0.10 apfu and is directly correlated to the amount of Ti in the crystals, due to an increase in the net charge of the crystal sites (Hill et al. 2000; Mollo et al. 2013). Clinopyroxene/silicate melt partitioning of Ti equilibrated under reducing conditions (below IW) is two to three times higher (0.2–0.3) than obtained in experiments where Ti^{4+} is exclusively present, which have $D_{Ti}^{cpx/melt} = 0.1–0.2$ (see Mallmann and O'Neill 2009; Leitzke

et al. 2016). Enstatite and forsterite had a maximum TiO_2 content of 1.43 wt% (0.04 apfu) and 0.14 wt%, respectively. Average olivine/silicate and opx/silicate melt partitioning values for Ti are also higher under reducing conditions ($D_{Ti}^{ol/melt} = 0.01$ and $D_{Ti}^{opx/melt} = 0.12$) when compared to oxidizing conditions, where $D_{Ti}^{ol/melt} = 0.006$ and $D_{Ti}^{opx/melt} = 0.06$ (Mallmann and O'Neill 2009) Basaltic glasses have TiO_2 contents ranging from 1.4 to 21.8 wt%, which cover almost the entire range observed in lunar mare basalts (see Meyer 2012; Warren and Taylor 2014) (Table 3).

Ti K-edge XANES spectra energy shifts, determination of Ti valence and coordination chemistry

Pre-edge and main edge features of the XANES K-edge spectra are a function of electronic transitions between bound states (Berry et al. 2003). For example, the pre-edge peak of the Ti K-edge XANES spectra is attributed to the transition from the 1s energy levels to bound 3d molecular orbitals (Grunes 1983; Waychunas 1987; Farges et al. 1996). Energy shifts on the XANES spectra are a function of oxidation state and coordination chemistry (e.g., Farges et al. 1997; Simon et al. 2007; Ackerson et al. 2017), with higher energies related to a higher oxidation state (Wong et al. 1984; Sutton et al. 1993; Berry et al. 2003). Titanium K-edge XANES spectra show a clear and consistent shift to lower energies for the absorption edge features obtained from standard reference materials with exclusively Ti^{4+} to metallic Ti (Table 4). The shift from Ti^{4+} to Ti^{3+} is more pronounced for oxides than it is for silicates in agreement with the findings of Waychunas (1987) and Sutton et al. (2017). For example, the energy shift observed between $CaTiSiO_5$ and $NaTi^{3+}Si_2O_6$ is 1.5 eV (Fig. 2), whereas the one seen between TiO_2 and Ti_2O_3 is 3 eV (Figs. 2, 3a, b). Several studies have shown that the most prominent pre-edge peak of the Ti K-edge XANES spectra, related to the 1s-3d transition, can be used to determine Ti valence (e.g., Waychunas 1987; Farges et al. 1997; Simon et al. 2007; Ackerson et al. 2017). To quantify the features of the XANES spectra obtained in our experiments, it was necessary to perform non-linear least square best fits to the line shapes. This procedure, although having little physical meaning, allows finding centroid positions, peak heights and areas, as well as to calculate the associated uncertainty. Peak fits were performed initially to the entire spectra dataset but this led to a large uncertainty, so it became necessary to produce peak fits specifically for the 1s-3d pre-edge peak to reduce the associated uncertainty. Because the energy centroid of the 1s-3d peak is strongly affected by background modelling, energy range and the function selected, we followed the method described in Berry et al. (2003) to perform the peak fitting. First, a baseline was defined as a straight line to cover the entire sloping area below the 1s-3d peak. Then, a spline function was used to define a curve through the 1s-3d absorption edge from ca. 5 eV before and after the expected centroid position (Fig. 4a–c). After that, a Lorentzian function was chosen to perform the non-linear least squares fits to each individual spectra in the 1s-3d peak selected range (generally 4966–4974 eV). The centroid energy position and uncertainty were then determined (Fig. 4a–c; Tables 4, 5, 6). The choice of the Lorentzian function used in the fits was because it produced better results when compared to pseudo-Voigt and Gaussian fits, as well as the expectation that electronic transitions follow a Lorentzian profile (Calas and Petiau 1983). The precision range of the fits was determined

Table 4 Position of the 1s-3d Ti K-edge and normalized absorption from XANES spectra obtained on reference materials in this study and selected literature data

Composition	Mineral	Ti valence	Source	References	1s-3d edge centroid peak position (eV)	Normalized peak absorption (E)
$FeTiO_3$	Ilmenite	4	Washington Pass, USA	This study	4970.9	0.23
Ti_3O_5	–	Mix	Alfa Aesar ® powder	This study	4970.2	0.15
TiO_2	Rutile	4	Horcajo de la Sierra, Spain	This study	4971.3	0.18
TiO_2	Brookite	4	Magnet Cove, USA	This study	4971.3	0.19
$CaTiSiO_5$	Titanite	4	Unknown location (Mineralogy Museum Bonn)	This study	4971.0	0.16
Ti_2O_3	–	3	Alfa Aesar ® powder	This study	4967.7	0.08
Ti	–	0	Alfa Aesar ® metal foil	This study	4966.8	0.41
Volcanic Glass	–	4	Columbia River Basalt, USA	Farges and Brown (1997)	4970.7	0.24
$NaTiSi_2O_6$	Pyroxene	3	Synthetic (Prewitt et al., 1972)	Sutton et al. (2017)	4969.5	0.07
$Mg_2(Si,Ti)O_4$	Olivine	4	Synthetic	Sutton et al. (2017)	4969.5	0.96
$(Ca,Na)(Mg,Fe,Al,Ti)(Si,Al)_2O_6$	Pyroxene	4	Synthetic	Sutton et al. (2017)	4970.4	0.10

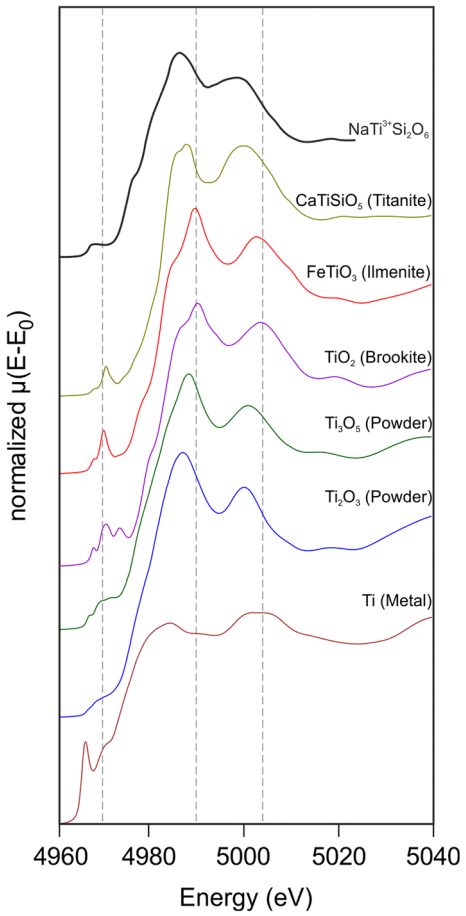

Fig. 2 Ti K-edge XANES spectra for standard reference materials plotted on normalized absorption ($E - E_0$) vs. energy (eV). Ti K-edge XANES spectra for $NaTi^{3+}Si_2O_6$, a synthetic pyroxene (Prewitt et al. 1972; Waychunas 1987), is shown for comparison. Guidelines are drawn to facilitate comparison between energy shifts

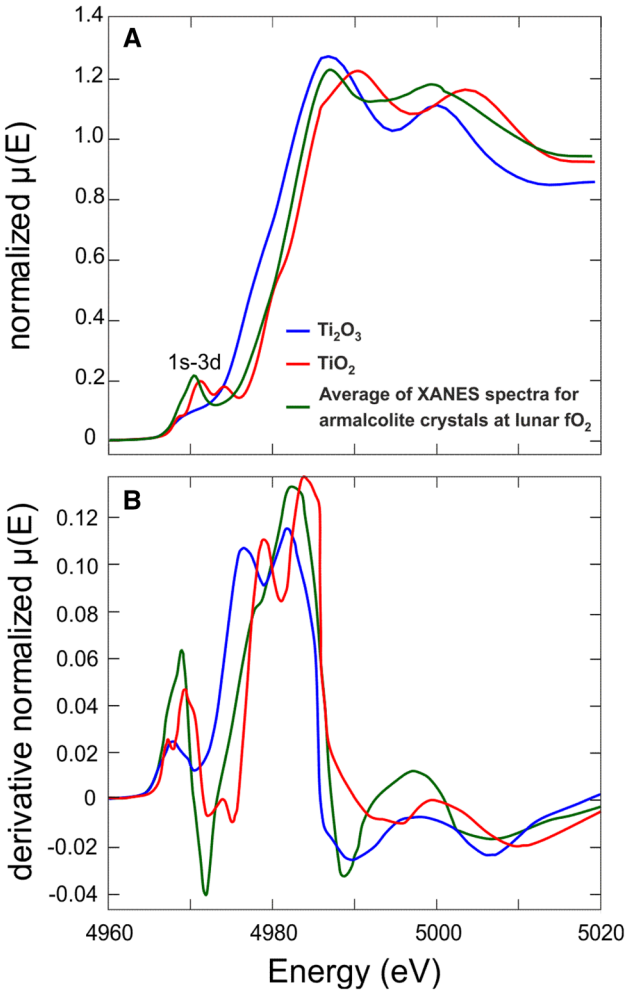

Fig. 3 **a** Normalized absorption and **b** derivative plotted vs. energy (eV) on a comparison between Ti K-edge XANES spectra for an average of all armalcolite crystals equilibrated below ΔIW-1.5 and two standard reference materials, showing the overall shift of 3 eV from TiO_2 to Ti_2O_3. Data shown in the plots was smoothed, but peak fitting and centroid calculation were performed on the raw data. For color-code in this figure legend, the reader is referred to the web version of this article

to be at maximum 5% for the normalized absorption value and 0.35 eV for the centroid peak energy (Tables 5, 6).

To determine the Ti coordination and oxidation of state in the experiments, the lever rule between standards representative of each one of the end-members was used (e.g., Sutton et al. 2017). For Fe–Ti oxides a direct comparison applying the lever rule between Ti K-edge XANES spectra for armalcolite and ilmenite and reference materials (TiO_2 and Ti_2O_3) could be done and valence was estimated based on the shift of the position of the 1s-3d peak centroid energy (Fig. 3). By comparing with appropriate reference materials, the coordination number of Ti^{3+} and Ti^{4+} in Fe–Ti oxides (armalcolite and ilmenite) in our study is [VI]-fold. Titanium valence ranges from 3.52 ± 0.08 to 3.87 ± 0.14 and the average valence (95% confidence) is of 3.63 ± 0.10 (i.e., Ti^{3+} from 27 to 47% of the total Ti) under fO_2 conditions relevant to lunar magmatism, i.e., between ΔIW-1.7 and -1.8 (Table 5; Fig. 5). Armalcolite crystals equilibrated under more oxidizing conditions, i.e., air and above the Fayalite-Magnetite-Quartz (FMQ) buffer showed Ti K-edge XANES spectra edge features similar to TiO_2 and $FeTiO_3$. Titanium valence calculated for these armalcolites is 3.9, indicating that mainly Ti^{4+} was incorporated in their crystal structure at oxidizing conditions.

In the silicates (pyroxene and olivine) the valence and coordination number of Ti was determined using the data and methodology described in Sutton et al. (2017) and Simon and Sutton (2018). The presence of Ti in both the tetrahedral and octahedral sites in the silicates (Fig. 6) requires an additional calibration step for first determining the contribution of each coordination and then the average valence. It is acceptable to use the data and the methodology from Sutton et al. (2017) to standardize our samples, since the settings used during

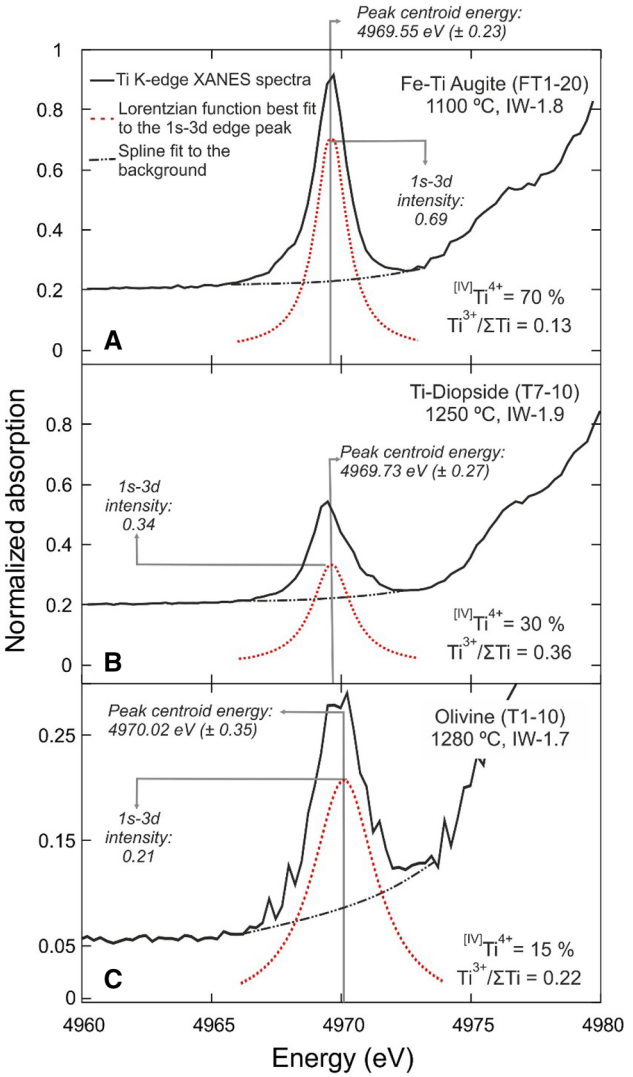

Fig. 4 Background subtracted and normalized Ti K-edge XANES spectrum with peak fits to the 1s-3d transition pre-edge feature and estimates of coordination number and oxidation state following Sutton et al. (2017). **A** Fe–Ti Augite crystal equilibrated at IW-1.8, 1100 °C with predominance of $^{[IV]}Ti^{4+}$ and Ti valence of 3.87; **b** Ti-diopside equilibrated at IW-1.9, 1250 °C with low proportion of $^{[IV]}Ti^{4+}$ and Ti valence of 3.64; **c** Olivine equilibrated at IW-1.7, 1280 °C with low proportion of $^{[IV]}Ti^{4+}$ and Ti valence of 3.78. Data for the plots is presented in Table 6. Raw data spectra are displaced in the *y*-axis to show the resulting best fit for each case

their XANES spectroscopy analysis were similar. Sutton et al. (2017) also acquired Ti K-edge XANES spectra using a Si (111) monochromator, as well as performing the energy calibration based on the first derivative peak energies in metal foil spectra (Ti = 4966 eV). Moreover, the method described in Sutton et al. (2017) has been successfully applied to lunar samples (Simon and Sutton 2018). In the silicates of our study (pyroxene and olivine), Ti^{3+} will occur exclusively in VI-fold coordination (Dowty and Clark 1973; Lombard et al. 2009), while Ti^{4+} can occur in IV or VI-fold coordination. The Ti^{4+} in tetrahedral coordination shows a high absorption intensity of the pre-edge peak (Farges et al. 1997) when compared to Ti^{4+} and Ti^{3+} in VI-fold coordination (Fig. 6). To account for the effect of IV-fold coordinated Ti^{4+} in the valence calculation we used the following end-member standards (Sutton et al. 2017): for IV-fold Ti^{4+} a synthetic forsterite produced in air (Energy: 4969.5 eV and normalized absorption: 0.96), and for VI-fold coordinated Ti^{4+} and Ti^{3+} natural (Energy: 4970.4 eV and normalized absorption: 0.10) and synthetic (Energy: 4969.5 eV and normalized absorption: 0.07) acmite crystals, respectively. After establishing each one of these end-members, each unknown measurement is plotted by a centroid-intensity point in the "$^{[IV]}Ti^{4+}$–$^{[VI]}Ti^{3+}$–$^{[VI]}Ti^{4+}$" mixing field (see Fig. 3 in Sutton et al. 2017). The proportion of $^{[IV]}Ti^{4+}$ is defined as the fractional intensity compared to that of the pure $^{[IV]}Ti^{4+}$ end-member and the remaining Ti fraction is assigned to "$^{[VI]}Ti^{3+}$ + $^{[VI]}Ti^{4+}$" by applying the lever rule again to the horizontal tie-line between the energies on the "$^{[IV]}Ti^{4+}$–$^{[VI]}Ti^{3+}$" mixing line and the "$^{[IV]}Ti^{4+}$–$^{[VI]}Ti^{4+}$" mixing curve at the measured intensity level (Sutton et al. 2017). By applying this method, Ti valence in silicates yield an average of 3.75 ± 0.16 (Ti^{3+} between 9–41% of the total Ti), ranging from 3.64 ± 0.09 to 3.90 ± 0.08 (Table 6; Fig. 6), with 1s-3d peak centroids ranging from 4969.52 to 4970.02 and normalized absorption from 0.21 (olivine) to 0.8 (cpx). Ti K-edge XANES spectra obtained in crystals from the same experiment and same conditions in our study show differences in their 1s-3d pre-edge centroid energies and normalized absorption (Fig. 6), which is related to the effect of crystal orientation (Ackerson et al. 2017). Some of our 1s-3d transition centroid energies lie outside the range defined by Sutton et al. (2017), which may be due to the nature of the fluorescence background, the function chosen to model the area under the pre-edge and the choice of the best-fit function (Berry et al. 2003). Additionally, we cannot entirely exclude that this is an effect of melt inclusions, even though the relation between crystal size and beam diameter should argue in favour of their absence. Pyroxenes and olivine in our study have a mixture between $^{[IV]}Ti^{4+}$–$^{[VI]}Ti^{3+}$–$^{[VI]}Ti^{4+}$, with a minimum of 16 and a maximum of 82% $^{[IV]}Ti^{4+}$ (Fig. 5b). Silicate glasses in equilibrium with the crystalline phases in our study show that Ti is exclusively tetravalent, with XANES spectra identical to the Columbia River Basaltic glass standard (Farges and Brown 1997), regardless of the fO_2 and of the starting composition.

Discussion and implications

The $Ti^{3+}/\Sigma Ti$ of minerals and magmas under lunar mantle conditions of fO_2

The redox transition between trivalent and tetravalent Ti is governed by the following reaction:

Table 5 Ti K-edge normalized absorption and peak position from XANES spectra obtained in this study

Composition	Phase	Temp. (°C)	ΔIW	1s-3d edge centroid energy (eV)	Uncertainty peak fit (±eV)	Normalized peak absorption	Ti valence	±	Ti coordination (average)
FT1-20	Arm	1100	− 1.8	4970.50	0.23	0.36	3.63	0.10	[VI]
T1-20	Arm	1260	− 1.7	4970.25	0.18	0.30	3.52	0.08	[VI]
T1-20	Arm	1260	− 1.7	4970.42	0.29	0.29	3.59	0.13	[VI]
T5-20	Arm	1260	− 1.7	4970.63	0.32	0.24	3.69	0.14	[VI]
T5-20	Arm	1260	10	4970.73	0.25	0.21	3.87	0.14	[VI]
T5-20	Arm	1260	3.4	4970.69	0.22	0.25	3.86	0.16	[VI]
T8-20	Arm	1260	− 1.7	4970.39	0.29	0.28	3.58	0.13	[VI]
T8-20	Arm	1260	− 1.7	4970.51	0.23	0.18	3.63	0.10	[VI]
FT1-10	Ilm	1100	− 1.8	4970.52	0.19	0.30	3.64	0.08	[VI]
FT1-10	Ilm	1100	− 1.8	4970.55	0.20	0.30	3.65	0.09	[VI]
FT1-10	Glass	1100	− 1.8	4970.23	0.11	0.35	4.00	0.04	[V]
FT1-10	Glass	1300	10	4970.28	0.17	0.35	4.01	0.06	[V]
FT1-10	Glass	1300	− 2.1	4970.30	0.14	0.35	4.02	0.05	[V]
FT1-20	Glass	1100	− 1.8	4970.21	0.12	0.35	3.99	0.04	[V]
FT1-5	Glass	1200	− 1.5	4970.21	0.13	0.36	3.99	0.04	[V]
FT1-5	Glass	1200	− 1.5	4970.24	0.16	0.36	4.00	0.05	[V]
T1-10	Glass	1300	10	4970.29	0.15	0.36	4.02	0.05	[V]
T1-10	Glass	1300	− 2.1	4970.24	0.16	0.36	4.00	0.05	[V]
T1-20	Glass	1260	− 1.7	4970.30	0.13	0.34	4.02	0.04	[V]
T5-20	Glass	1260	− 1.7	4970.25	0.17	0.36	4.00	0.05	[V]
T5-20	Glass	1260	10	4970.21	0.16	0.35	3.99	0.05	[V]
T5-20	Glass	1260	3.4	4970.27	0.13	0.36	4.01	0.04	[V]
T5-20	Glass	1260	− 1.7	4970.35	0.15	0.34	4.03	0.05	[V]
T7-10	Glass	1250	− 1.9	4970.28	0.17	0.36	4.01	0.06	[V]
T7-20	Glass	1300	10	4970.28	0.13	0.35	4.01	0.04	[V]
T7-20	Glass	1300	− 2.1	4970.24	0.14	0.34	4.00	0.04	[V]
T7-5	Glass	1250	− 1.9	4970.30	0.15	0.36	4.02	0.05	[V]
T8-20	Glass	1260	− 1.7	4970.26	0.12	0.38	4.01	0.04	[V]

Calculated valence is shown for silicate glasses and Fe–Ti oxides, which have Ti average in [V] and [VI]-fold coordination, respectively

$$TiO_{1.5} + 1/4\ O_2 = TiO_2 \quad (1)$$

which has an equilibrium constant (K_{eq}) expressed by the division between the activities of the products by the activities of the reactants:

$$-\frac{\Delta G^0_{(1)}}{RT} = \ln K_{eq} = \ln \frac{(a\mathrm{TiO_2})}{\left(a\mathrm{TiO_{1.5}}\right) \cdot (f\mathrm{O_2})^{1/4}} \quad (2)$$

If equilibrium (1) involves pure phases, solving Eq. (2) to obtain fO_2 yields values that range from 10^{-28} to 10^{-25} bars at mantle magmatic temperatures (1000–1400 °C), which is about 12 log units more reduced than the Fe–FeO redox equilibrium. However, these redox conditions are not realistic for a magmatic system, where it is clear that the composition of the magma (namely SiO_2 content) and the crystal chemistry and stoichoimetry will change the chemical activities of TiO_2 and $TiO_{1.5}$ in silicate melt when compared to pure substances (see O'Neill and Eggins 2002; Borisov 2012). Schreiber (1986) showed that in glass-forming melts the base composition determines the polymerization of the melt and the amount of free oxide ions released to the melt (i.e., the oxide ion activity) to participate in the redox kinetics. Any change in the activity coefficients of the Ti oxide species will be associated with a shift of the redox transition of Ti^{4+} to Ti^{3+} to different values of fO_2. For example, $Ti^{3+}/\sum Ti$ estimates based on a mineral composition from silicates in Ca–Al coarse-grained refractory inclusions, which were formed in a highly reduced solar nebula, set the $TiO_{1.5}$–TiO_2 redox equilibrium at IW-7 (Simon et al. 2007; Grossmann et al. 2008; Papike et al. 2016; Sutton et al. 2017), while in silicate glasses at 1500 °C the $Ti^{3+}/\sum Ti$ obtained using redox titration ranges from 0.9 at IW− 11 to 0.1 at IW-3 (Schreiber and Balasz 1982; Schreiber 1986).

Table 6 Ti K-edge normalized absorption and peak position from XANES spectra obtained in this study

Composition	Phase	Temp. (°C)	ΔIW	1s-3d edge centroid energy (eV)	Uncertainty peak fit (±eV)	Normalized peak absorption	Ti valence	±	$^{[IV]}Ti^{4+}$ (%)
FT1	Cpx	1200	− 1.5	4969.65	0.25	0.45	3.70	0.08	42
FT1-10	Cpx	1100	− 1.8	4969.62	0.20	0.52	3.77	0.06	50
FT1-10	Cpx	1100	− 1.8	4969.75	0.26	0.34	3.67	0.09	30
FT1-10	Cpx	1100	− 1.8	4969.54	0.28	0.62	3.73	0.09	62
FT1-10	Cpx	1100	− 1.8	4969.55	0.23	0.64	3.79	0.07	64
FT1-10	Cpx	1100	− 1.8	4969.54	0.19	0.71	3.87	0.06	72
FT1-20	Cpx	1100	− 1.8	4969.55	0.23	0.69	3.87	0.07	70
FT1-5	Cpx	1200	− 1.5	4969.76	0.27	0.34	3.69	0.09	30
FT1-5	Cpx	1200	− 1.5	4969.60	0.24	0.49	3.67	0.08	47
FT1-5	Cpx	1200	− 1.5	4969.65	0.20	0.47	3.74	0.06	45
T7-10	Cpx	1250	− 1.9	4969.78	0.19	0.32	3.68	0.04	28
T7-10	Cpx	1250	− 1.9	4969.73	0.27	0.34	3.64	0.09	30
T7-10	Cpx	1250	− 1.9	4969.54	0.25	0.71	3.87	0.08	72
T7-5	Cpx	1250	− 1.9	4969.52	0.24	0.80	3.90	0.08	82
T7-5	Cpx	1250	− 1.9	4969.75	0.32	0.35	3.69	0.10	31
T1-10	Olv	1280	− 1.7	4970.02	0.35	0.21	3.78	0.12	16
T5-20	Opx	1260	− 1.7	4969.70	0.26	0.38	3.67	0.08	35
T5-20	Opx	1260	− 1.7	4969.75	0.18	0.34	3.67	0.06	30

Calculated valence is shown for silicates (pyroxene and olivine), which have a mixture between [IV] and [VI]-fold coordination. The proportion of $^{[IV]}Ti^{4+}$ was determined following the methodology of Sutton et al. (2017)

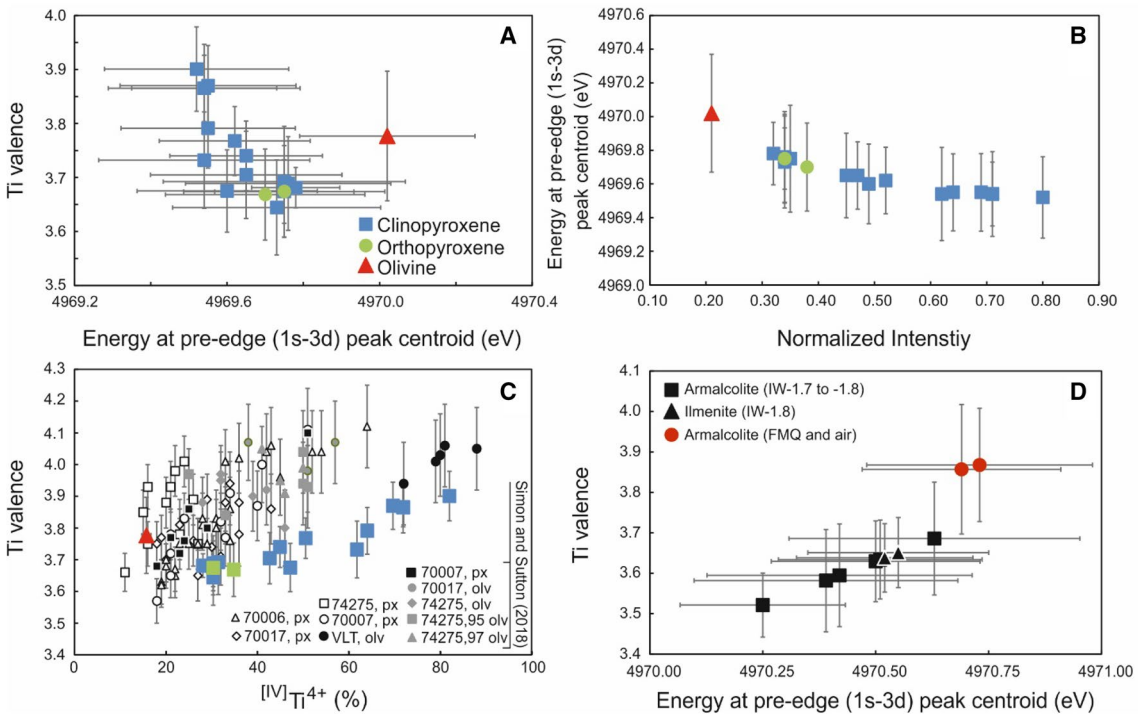

Fig. 5 **a**–**c** Ti valence and coordination number obtained employing the calibration method of Sutton et al. (2017) using peak centroid energy position and normalized absorption for silicates; **d** Ti valence in Fe–Ti oxides at different fO_2

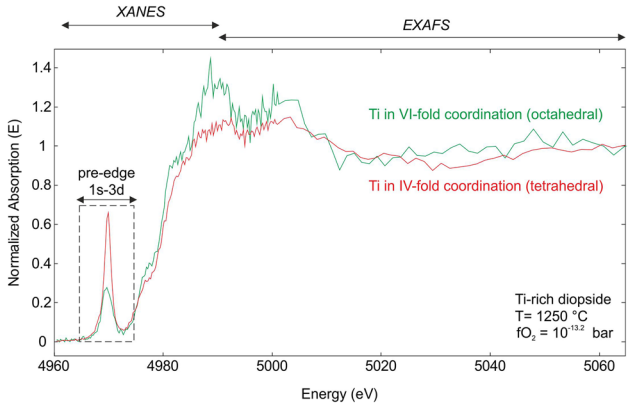

Fig. 6 Example of Ti K-edge X-ray absorption spectroscopy (XAS) signals obtained in fluorescence mode for Ti-rich clinopyroxene crystals showing different areas and features of the spectra, including the X-ray absorption near edge structure (XANES) region and the beginning of the Extended X-ray absorption fine structure (EXAFS) region. Titanium is shown here in two different crystals of the same experiment where Ti occurs with mixed valence, where there was predominance of VI-fold coordination (green) and IV-fold coordination (red)

Direct XANES Ti K-edge measurements of pyroxene and olivine from lunar samples originated under reducing conditions have reported $Ti^{3+}/\sum Ti$ values of 0.1–0.4 (Sung et al. 1974; Simon et al. 2014; Simon and Sutton 2017, 2018). Some of these values are discrepant, albeit within error of those reported in our study, which can be explained in two ways: (1) the fO_2 imposed by the experimental atmosphere is a major control of the activity coefficient (γ) of both Ti redox species, which will change the activity of these species in the silicate melt; and (2) the major element composition of basaltic glasses in our study is substantially different from that found in CAI-inclusions (see Simon et al. 2007), as well as the mechanism of formation of both rocks. Simon and Sutton (2017, 2018) reported valences for lunar pyroxenes and olivines ranging from 3.66 to 4.15, with maximum $^{[IV]}Ti^{4+}$ of 88% in lunar olivine. Additionally, Simon and Sutton (2018) argue that Ti valence results obtained by their calibration that are above 4 reflect the lack of orientation correction for crystals with Ti^{4+} mainly in highly asymmetric sites (IV-fold). Moreover, given that some of the values are outside the range, albeit within error, of values reported by Sutton et al. (2017) may indicate some small amount of glass contamination during the measurement, or be related to the differences in background subtraction and peak fitting procedure. Although the valence obtained in the silicates of our study (Fig. 5b) being in general agreement with Simon and Sutton (2017, 2018), our results do not show a large amount of tetrahedrally coordinated Ti in olivine, but do show larger amounts in the pyroxene (up to 78% $^{[IV]}Ti^{4+}$). This may be related to the fact that the crystals in our study are more Ti-rich and Fe-poor than the natural lunar pyroxene, albeit with similar Al content. When compared to experimental results on equivalent compositions, our valence estimate for Ti in pyroxene, which range from 3.64 to 3.90 are within error to those obtained by Krawczynski et al. (2010), who report a lower limit of 3.5 for pyroxenes equilibrated at ΔIW-2. Tetravalent titanium may be present in either lower symmetry sites (IV-fold coordination—tetrahedral site) or higher symmetry sites (VI-fold coordination—M1 octahedral site) in the clinopyroxene, with the former occurring more often in crystals equilibrated at high-temperature, low pressure and small amounts of Al^{3+} available for charge balancing coupled substitutions (see Sepp and Kunzmann 2001; Nazzareni et al. 2004; Simon et al. 2014). Lunar pyroxene has crystallized mainly from Al-poor magmas, and, hence, can have up to 50% of the total Ti in IV-fold coordination (Simon et al. 2014), which is in agreement with our experimental proxies.

Lunar magmas are expected to become progressively enriched in Ti^{4+} as fractional crystallization progresses, with Ti^{3+}/Ti^{4+} content of pyroxene decreasing with increasing ferrosilite content in the most reduced lunar rocks (Taylor et al. 2004; Simon and Sutton 2017), because Ti^{3+} is retained at the source due to its higher crystal/silicate melt compatibility under lower conditions of fO_2 (see Connolly and Burnett 2003; Mallmann and O'Neill 2009). This seems to be also the case in our experiments, because all of the Ti^{3+} present in the system has been identified in the crystalline phases, whereas the silicate glass appears to exclusively contain Ti^{4+} in V-fold coordination, with XANES spectra identical to the Columbia River Basaltic glass standard (Farges and Brown 1997), regardless of the initial starting composition. Another possible explanation for the presence of exclusively Ti^{4+} in the glass would be a redox exchange with C dissolved in silicate melt from the CO–CO_2 gas mixture used during the experiments, but this possibility needs to be tested. Nevertheless, the solubility of C in silicate melts at 1 bar is so small (less than 1 ppm—see Ni and Keppler 2013), that it is unlikely enough C would be available to effect the necessary redox exchange with Ti^{3+}.

Trivalent titanium is exclusively in VI-fold coordination due to its larger radius and the fact that the substitution of Ti^{3+} for a divalent cation in the M1 site requires only the substitution of one other atom at the tetrahedral (T) site (Al^{3+} for Si^{4+}) (Papike et al. 2005; Simon et al. 2007). The substitution of trivalent Ti at the M1 site of clinopyroxene under extremely reduced conditions has also been described in CAI inclusion of the Allende Meteorite, with grossmanite ($CaTi^{3+}AlSiO_6$) as the end-member of this solid-solution (Ma and Rossman 2009b). In forsterite crystals, both atomistic calculations and XANES measurements have shown that the substitution of Ti^{4+} by Si^{4+} in the T-site (Mg_2TiO_4) is favoured in comparison to Ti^{4+} for Mg^{2+} in the M1 site, which requires formation of a vacancy or substitution of

Mg^{2+} for Si^{4+} at the T-site (Berry et al. 2007). Curiously in our experiments, the intensity of the 1s-3d transition feature in olivine corresponds to the one expected exclusively for VI-fold coordination, albeit with lower absorption energy (4970.22 eV) when compared to $^{[VI]}Ti^{4+}$ (4971 eV—see Berry et al. 2007). The reason for that may be the mixture of valences, with presence of a significant amount of Ti^{3+} in olivine below IW-1.5, which will be exclusively in VI-fold coordination, in addition to $^{[IV]}Ti^{4+}$ (Berry et al. 2007).

Most of the Ti enrichment in lunar mare basalts is hosted by Fe–Ti oxides (Meyer 2012). Previous microprobe-based estimates of Ti^{3+} for lunar Fe–Ti oxides (e.g., Pavicevic et al. 1972; Stanin and Taylor 1980) pointed to a whole-rock $Ti^{3+}/\sum Ti$ ratio of 0.1–0.2, which is within error of the ones obtained by our X-ray absorption spectroscopic measurements. Wet chemistry measurements also give a range of 4–10 mol% of the so-called "anosovite" component ($Ti_2^{3+}TiO_5$) in lunar armalcolites (Wechsler et al. 1975). Borisov et al. (2004) performed experiments in synthetic Al-bearing karrooites and obtained $Ti^{3+}/\sum Ti$ ranging from 0.2 to 0.4, with whole-rock $\left[Ti^{3+}/\sum Ti\right]_T$ of 0.1 at 1300 °C and $\log fO_2$ between − 11 and − 12, which is in good agreement with our data. Simons and Woermann (1978) studied the Fe–Ti-O system and found out through wet chemistry that armalcolite as well as ilmenite and ulvite ($TiFe_2O_4$) at temperature above 1200 °C, pressure of 1 bar and in equilibrium with metallic iron, always have Ti^{3+}, which explains the excess of Ti in lunar oxide minerals compared to what is expected if only Ti^{4+} was present (El Goresy et al. 1972). The substitution of Ti^{3+} in ilmenite extends the solid solution Fe_2O_3–$FeTiO_3$ beyond the stoichiometric ratio of Ti/Fe = 1, in direction of the stability of Ti_2O_3 (Simons and Woermann 1978). In addition, the effect of crystal and melt composition also play a major role on affecting the redox transition of Ti, and therefore, the stability of Ti^{3+} rich oxide minerals (Kesson and Lindsley 1975). For example, while ferropseudobrookite is only stable at 1 bar above 1060 °C (Simons and Woermann 1978), it becomes stable with the addition of trivalent cations such as Al^{3+}, Cr^{3+}, and Ti^{3+} down to 850 °C (Kesson and Lindsley 1975), which can also explain the high amount of $Ti^{3+}/\sum Ti$ in our experiments.

First principles modelling and implications for mass-dependent Ti stable isotope fractionation in the context of lunar magmatism

Mass-dependent isotope fractionation during magmatic processes is mainly controlled by variations in the coordination number and in the bonding environments of the coexisting phases. For example, the lighter isotope of a given element is expected to preferentially substitute into higher coordinated sites, which exhibit a longer cation–anion bond length and weaker bond strength, whereas the heavier isotope shows the opposite behaviour (Schauble et al. 2009; Wunder et al. 2011; Kowalski et al. 2013). There is some precedent for redox-dependent stable isotope fractionation during magmatic processes. For example, there is a resolvable difference between the $\delta^{56}Fe$ of mid-ocean ridge basalts (MORB) samples in relation to their mantle sources, where the former are clearly isotopically heavier than the latter (Dauphas et al. 2014). Dauphas et al. (2014) argued that the reason for this decoupling is due to mantle melts having higher ferric/ferrous iron ratios when compared to their mantle sources, leading to a fractionation in $\delta^{56}Fe$ of 0.1‰. The perceived difference in redox environment in the sources of low- and high-Ti mare basalts is important for two reasons: (1) high-Ti basalt sources may be reduced enough such that Ti^{3+} may be present in addition to the more typical Ti^{4+} (Krawczynski et al. 2009; Simon and Sutton 2018; and findings of our study); (2) any redox-dependent changes in the coordination environment of Ti, in either silicate melt or any residual lunar mantle phases, can potentially affect the fractionation of stable isotopes of Ti during lunar mantle melting. This expectation is partly supported by the observation that high-Ti basalts can show higher $\delta^{49}Ti$ (+ 0.03‰) than low-Ti basalts (− 0.01‰), the later having a Ti isotope composition similar to the bulk-silicate Earth (BSE) average, as calculated by Millet et al. (2016) using a double spike technique that has an uncertainty of ± 0.02‰ at 95% confidence (for details see Millet and Dauphas 2014). If during the petrogenesis of high-Ti basalts, Ti^{3+} is similarly decoupled from Ti^{4+}, this could explain why high-Ti basalts are isotopically heavier than low-Ti basalts by about 0.03‰ (Millet et al. 2016). Petrogenetic models of high-Ti basalts have suggested that they were originated under more reducing conditions when compared to low-Ti basalts due to two main reasons: (1) the necessity of considering residual metal at their source to reproduce lithophile–siderophile trace element trends, such as Hf/W, Th/W and Ta/W (Fonseca et al. 2014; Leitzke et al. 2016); (2) the fact that olivines from high-Ti basalts are so much more depleted in Ni when compared to olivines from low-Ti basalts (~ 20 and ~ 400 µg/g respectively; Karner et al. 2003). In low-Ti basalts, which would have formed under more oxidizing conditions than high-Ti basalts, and result from higher degrees of partial melting, Ti may be exclusively tetravalent and no such redox decoupling can take place. As a result, the $\delta^{49}Ti$ of low-Ti basalts should more closely reflect their mantle sources, which are themselves close to BSE (Zhang et al. 2012). Therefore, studies dealing with the estimation of $Ti^{3+}/\sum Ti$ and Ti coordination number in minerals equilibrated under conditions of fO_2 relevant to the lunar mantle are specifically important to understand the origin of lunar mare basalts and the resolvable differences in the Ti isotope composition of terrestrial and lunar samples (Millet et al. 2016).

To illustrate the relation between our structural data and Ti isotope signatures, we have carried out ab initio calculations, based on density-functional theory (DFT), of mass-dependent Ti equilibrium isotope fractionation (Fig. 7) between different Ti oxidation states (3 + and 4 +) and coordination environments (IV and VI-fold coordination) in karrooite and clinopyroxene. Mass-dependent equilibrium isotope fractionation is governed by the variation in molecular and crystalline vibrational frequencies, which depend on the strength of chemical bonds as well as on the masses of individual atoms and their isotopes. The fractionation factor β describes the theoretical isotope fractionation between the bonding environment in the phase of interest (e.g., tetrahedral or octahedral crystal site) and an ideal monatomic gas of the element of interest (Bigeleisen and Mayer 1947; Urey 1947; Chacko et al. 2001). In general, the calculation of the β-factor for a crystal or a glass is complex and requires substantial computational resources due to the need to compute the full vibrational spectrum of a complex multiparticle system. At high temperatures, the calculation of the β-factor can be approximated by an expression that requires only the knowledge of the three force constants that act upon the fractionating element and the respective isotope masses (Bigeleisen and Mayer 1947):

$$\beta = 1 + \frac{\Delta m}{m m^*} \frac{\hbar^2}{24 K_B^2 T^2} \sum_{i=1}^{3} A_i, \tag{3}$$

where A_i are the force constants acting on the isotopic atom in the three perpendicular spatial directions (x, y and z), $\Delta m = m^* - m$, where m and m^* are the masses of the lighter and heavier isotopes of the fractionating element, $\hbar$ is the reduced Planck constant, K_B is the Boltzmann constant and

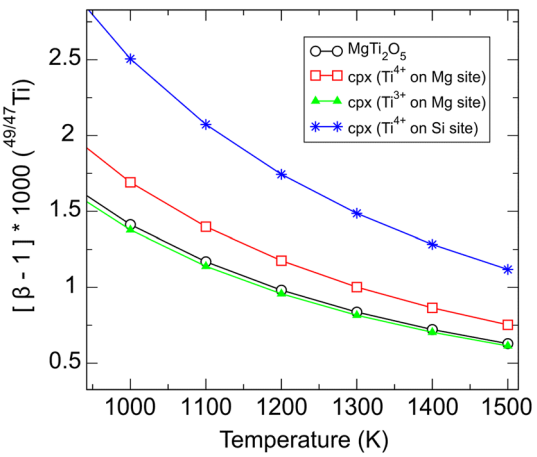

Fig. 7 Results of ab initio simulations of mass-dependent Ti equilibrium isotope fractionation factors (β) in karrooite and pyroxene (diopside) considering different Ti oxidation states (3 + and 4 +) and coordination numbers (IV and VI-fold coordination)

T is temperature (K). Here, we computed the β-factor using an extension to the Bigeleisen and Mayer approximation as proposed by Kowalski et al. (2013), described by the following equation:

$$\beta = \prod_{i=1}^{3} \frac{u_i^*}{u_i} \exp\left[\frac{u_i - u_i^*}{2}\right] \frac{1 - \exp\left(-u_i\right)}{1 - \exp\left(-u_i^*\right)} \tag{4}$$

Here, $u_i = h\bar{\upsilon}_i / K_B T$ with $\bar{\upsilon}_i = A_i / 4\pi^2 m$ are the so-called "pseudo-frequency" corresponding to force constant A_i. All calculations were made with the DFT code ABINIT (Gonze et al. 2016) using the local density approximation for the exchange–correlation functional and Troullier–Martins-type pseudopotentials (Troullier and Martins 1991). The planewave basis set for expanding the Kohn–Sham orbitals were cut off at an energy of 1000 eV. The reciprocal space was sampled using a suitable Monkhorst–Pack k-point grid. In a first step, lattice parameters and atomic positions of the crystal structures were optimized. As the calculation of force constants A_i of the isotopic atom requires simulation cells that are large enough to avoid significant interaction between periodic images arising due to periodic boundary conditions, we used supercells of the crystal unit cells, i.e., a 2 × 1 × 1 supercell of the orthorhombic structure (space group Cmcm) of karrooite with 64 atoms and a 1 × 1 × 2 supercell of diopside (monoclinic, space group C2/c) with 80 atoms. This ensured a minimum simulation cell dimension of 7.5 Å in any direction. For the incorporation of Ti into the pyroxene structure we studied three different mechanisms: (1) the replacement of one Si by Ti^{4+} on the tetrahedral site, (2) the replacement of one Mg by Ti^{3+} charge-compensated by the replacement of one Si by one Al, and (3) the replacement of one Mg by Ti^{4+} charge-compensated by the replacement of two Si by two Al atoms. After the replacements a new structure optimization was performed. In the next step, the isotopic atom (Ti^{4+} or Ti^{3+}) was displaced by 0.01 Å in the three Cartesian directions and the induced forces were computed. Finally, the later were transformed into force constants A_i (= force divided by displacement) and pseudo-frequencies $\bar{\upsilon}_i$, from which the β-factor was computed according to Eq. (4). The resulting β-factors are shown in Fig. 7 as a function of temperature.

The predicted mass-dependent Ti equilibrium isotope fractionation factors (β) suggest that for phases like karrooite and pyroxene at magmatic temperatures the main factor controlling this process in the crystals is the coordination chemistry of Ti. The largest fractionation factor is observed when Ti^{4+} is incorporated into pyroxene replacing Si (Fig. 7), which may occur in Al-poor systems in nature (e.g., Quartieri et al. 1993; Nazzareni et al. 2004), as observed for lunar pyroxenes (e.g., Papike et al.

2005; Simon et al. 2014; Simon and Sutton 2017, 2018). When compared solely with the coordination chemistry, the Ti oxidation state plays a minor role in the fractionation factor relative to a monoatomic Ti gas phase, tending to lighter Ti isotopic compositions with lower oxidation state (Fig. 7). The local crystal structure also affects the fractionation factor, given that tetravalent Ti in VI-fold coordination in karrooite ($MgTi_2O_5$) and pyroxene show different fractionation factors. A quantitative comparison of our results to observed Ti stable isotope fractionation in natural samples is not possible at this stage because we have not attempted to compute the fractionation factor β for the silicate glass. This would require a more dedicated and systematic computational study, which is beyond the scope of this paper. The observation that the average coordination chemistry of Ti in the silicate glass is V-fold suggests that if partial melting occurs with a residue that has crystals predominantly with IV-fold coordinated Ti, the melt will be isotopically lighter, while the opposite may happen if crystals are predominantly with VI-fold coordinated Ti. Experimental and computational studies for other isotopic systems (e.g., Li) have shown, however, that the coordination-principle may not be applicable to every isotope fractionation process, and bond valence models can provide more realistic scenarios (Wunder et al. 2011). As such, additional experimental constraints are still necessary to test this hypothesis for Ti isotope fractionation.

Concluding remarks

We have reported a broad dataset of micro-XANES spectroscopic Ti K-edge measurements on synthetic lunar minerals and basaltic glasses under reduced fO_2 conditions, especially important for the petrogenesis of lunar rocks. Our results allowed investigating the redox state and coordination environment of titanium in silicate glasses and crystals in experiments equilibrated below the Fe–FeO redox buffer at magmatic temperatures. The average valence for Ti is 3.6, i.e., a 40% portion of Ti^{3+} for Fe–Ti oxides (ilmenite and armalcolite) under fO_2 conditions relevant to lunar magmatism (IW − 1.5 to − 1.8). Pyroxenes and olivine have average Ti valence of 3.75 with up to 82% IV-fold coordinated Ti, while silicate glasses show XANES Ti K-edge spectra consistent with the presence of exclusively tetravalent Ti. In addition, our new results are applied to provide first insights into the mechanisms that may control Ti mass-dependent equilibrium isotope fractionation in lunar mare basalts (Millet et al. 2016), albeit being difficult to apply directly to nature, mainly because the fractionation factor β for the glass is difficult to calculate due to its complex structure. The main challenge would be to produce a realistic structure model for the glass, which would yield the statistical distribution of different Ti coordination environments. Nevertheless, the observation that coordination chemistry is likely to be the main factor affecting Ti mass-dependent equilibrium isotope fractionation in magmatic systems can be used to assert that a silicate glass with average Ti in V-fold coordination will be isotopically distinct from the crystals, which have Ti predominates at IV and VI-fold coordination. Our experiments, however, failed to produce a silicate glass with detectable Ti^{3+}, which may occur in a different coordination environment than Ti^{4+}. Therefore, future experimental work is required to perform in situ XANES Ti K-edge measurements in experiments with crystals and silicate glass at different fO_2, such as the ones performed for Fe oxidation state using an aerodynamic levitation laser-heated system combined with a chamber and gas mixing (Aldermann et al. 2017), multi-anvil apparatus or gas-mixing high-temperature furnaces adapted for using coupled into a beamline synchrotron facility (e.g., Wilke et al. 2007; Rushmer et al. 2015; Mallmann et al. 2016). As a final remark, the data presented here can be coupled to other redox sensitive elements (e.g., V, Fe, and Cr) to constrain via oxybarometry the magmatic evolution of the Moon, and by inference, of any other differentiated planetary body in the solar system (e.g., Karner et al. 2006; Simon and Sutton 2017, 2018).

Acknowledgements We thank all colleagues at the University of Bonn and University of Cologne, and at the ANKA Synchrotron facility in the Karlsruhe Institute of Technology, especially D. Lülsdorf, T. Schulz, N. Jung and H. Blanchard for the technical support. We are also grateful to C. Ballhaus and S. Aulbach for discussion of the results, as well as S. Sutton for valuable insights into the Ti valence determination. Editor J. Hoefs and the anonymous referees are acknowledge for their constructive input. F.P.L. was supported by a PhD. scholarship from the Brazilian National Council for Scientific and Technological Development (DAAD/CNPq-grant 248562/2013-4). R.F. acknowledges research funding from the Deutsche Forschungsgemeinschaft (DFG—Grants FO 698/5 and FO 698/6).

References

Ackerson MR, Tailby ND, Watson EB (2017) XAFS spectroscopic study of Ti coordination in garnet. Am Miner 102:173–183

Aldermann OLG, Wilding MC, Tamalonis A, Sendelbach S, Heald SM, Benmore CJ, Johnson CE, Johnson JA, Hah HY, Weber JKR (2017) Iron K-edge X-ray absorption near-edge structure spectroscopy of aerodynamically levitated silicate melts and glasses. Chem Geol 453:169–185

Ballhaus C (1993) Redox states of lithospheric and asthenospheric upper mantle. Contrib Miner Petrol 114:331–348

Beard BL, Taylor LA, Scherer EE, Johnson CM, Snyder GA (1998) The source region and melting mineralogy of high-titanium and low-titanium lunar basalts deduced from Lu–Hf isotope data. Geochim Cosmochim Acta 62:525–544

Berry AJ, O'Neill HSTC (2004) A XANES determination of the oxidation state of chromium in silicate glasses. Am Miner 89:790–798

Berry AJ, O'Neill HSTC, Jayasuryia KD, Campbell SJ, Foran GJ (2003) XANES calibrations for the oxidation state of iron in a silicate glass. Am Miner 88:967–977

Berry AJ, Walker AM, Hermann J, O'Neill HSTC, Foran GJ, Gale JD (2007) Titanium substitution mechanisms in forsterite. Chem Geol 242:176–186

Bigeleisen J, Mayer MG (1947) Calculation of equilibrium constants for isotopic exchange reactions. Journal of Chemical Physics 15:262–267

Borisov AA (2012) The Ti^{4+}/Ti^{3+} ratio of magmatic melts: application to the problem of the reduction of lunar basalts. Petrology 20:391–398

Borisov AA, Brenker F, Palme H (2004) Liquidus karrooite stability and composition at reducing conditions. Contrib Miner Petrol 148:69–78

Borisov A, Behrens H, Holtz F (2013) The effect of titanium and phosphorous on ferric/ ferrous ratio in silicate melts: an experimental study. Contrib Miner Petrol 166:1577–1591

Brophy JG, Basu A (1990) Europium anomalies in mare basalts as a consequence of mafic cumulate fractionation from an initial lunar magma ocean. In: Proceedings of the 20th lunar and planetary science conference, pp 25–30

Calas G, Petiau J (1983) Coordination of iron in oxides glasses through high-resolution K-edge spectra: information from the pre-edge. Solid State Commun 48:625–629

Chacko T, Cole DR, Horita J (2001) Equilibrium oxygen, hydrogen and carbon isotope fractionation factors applicable to geologic systems. Rev Mineral Geochem 43:1–81

Connolly HC Jr, Burnett DS (2003) On type B CAI formation: experimental constraints on fO_2 variations in spinel minor element partitioning and reequilibration effects. Geochim Cosmochim Acta 67:4429–4434

Dauphas N, Roskosz M, Alp EE, Newville DR, Hu MY, Sio CK, Tissot FLH, Zhao J, Tissandier L, Médard E, Cordier C (2014) Magma redox and structural controls on iron isotope variations in Earth's mantle and crust. Earth Planet Sci Lett 398:127–140

DesMarais DJ, Hayes JM, Meinschein WG (1972) Pyrolysis study of carbon in lunar fines and rocks. In: The Apollo 15 lunar samples. Lunar Science Institute, Houston, pp 294–297

Donaldson CH, Williams RJ, Logfren GE (1975) A sample holding technique for study of crystal growth in silicate melts. Am Miner 60:324–326

Dowty E, Clark JR (1973) Crystal structure refinement and optical properties of a Ti^{3+} fassaite from the Allende meteorite. Am Mineral 58:230–242

Dyl KA, Simon JI, Young ED (2011) Valence state of titanium in the Wark-Lovering rim of a Leoville CAI as a record of progressive oxidation in the early Solar Nebula. Geochim Cosmochim Acta 75(3):937–949

El Goresy A, Ramdohr P, Taylor LA (1972) Fra Mauro crystalline rocks: mineralogy, geochemistry, and subsolidus reduction of the opaque minerals. In: Proceedings of the 3rd lunar science conference, p 33

Farges F, Brown GE Jr, Rehr JJ (1996) Coordination chemistry of Ti (IV) in silicate glasses and melts: I. XAFS study of titanium coordination in oxide model compounds. Geochim Cosmochim Acta 60:3023–3038

Farges F, Brown GE Jr (1997) Coordination chemistry of titanium (IV) in silicate glasses and melts: IV. XANES studies of synthetic and natural volcanic glasses and tektites at ambient temperature and pressure. Geochim Cosmochim Acta 61:1863–1870

Farges F, Brown GE Jr, Rehr JJ (1997) Ti K-edge XANES studies of Ti coordination and disorder in oxide compounds: comparison between theory and experiment. Phys Rev B 56:1809–1819

Farges F, Wilke M (2015) Planetary, geological and environmental sciences. In: van Bokhoven JA, Lamberti C (eds) XAS and XES: theory and applications, vol II. Wiley, Oxford, pp 561–608

Fonseca ROC, Mallmann G, Sprung P, Sommer JC, Heuser A, Speelmanns IM, Blanchard H (2014) Redox controls on tungsten and uranium crystal/silicate melt partitioning and implications for the U/W and Th/W ratio of the lunar mantle. Earth Planet Sci Lett 404:1–13

Frost DJ, McCammon CA (2008) The redox state of the Earth's mantle. Annu Rev Earth Planet Sci 36:389–420

Gonze X, Jollet F, Abreu Araujo F, Adams D, Amadon B, Applencourt T, Audouze C, Beuken J-M, Bieder J, Bokhanchuk A, Bousquet E, Bruneval F, Caliste D, Côté M, Dahm F, Da Pieve F, Delaveau M, Di Gennaro M, Dorado B, Espejo C, Geneste G, Genovese L, Gerossier A, Giantomassi M, Gillet Y, Hamann DR, He L, Jomard G, Laflamme Janssen J, Le Roux S, Levitt A, Lherbier A, Liu F, Lukačević I, Martin A, Martins C, Oliveira MJT, Poncé S, Pouillon Y, Rangel T, Rignanese G-M, Romero AH, Rousseau B, Rubel O, Shukri AA, Stankovski M, Torrent M, Van Setten MJ, Van Troeye B, Verstraete MJ, Waroquiers D, Wiktor J, Xu B, Zhou A, Zwanziger (2016) Recent developments in the ABINIT software package. JW Comput Phys Commun 205:106–131

Grossmann L, Beckett JR, Fedkin AV, Simon SB, Ciesla FB (2008) Redox conditions in the solar nebula: observational, experimental, and theoretical constraints. Rev Mineral Geochem 68:93–140

Grunes LA (1983) Study of the K edges of 3d transition metals in pure and oxide form by x-ray-absorption spectroscopy. Phys Rev B 27:2111

Hill E, Wood BJ, Blundy JD (2000) The effect of Ca-Tschermaks component on trace element partitioning between clinopyroxene and silicate melt. Lithos 53:203–215

Joly Y, Grenier S (2016) Theory of X-ray absorption near edge structure. In: van Bokhoven JA, Lamberti C (eds) X-ray absorption and X-Ray emission spectroscopy: theory and applications. Wiley, Oxford, pp 73–95

Karner J, Papike JJ, Shearer CK (2003) Olivine from planetary basalts: chemical signatures that indicate planetary parentage and those that record igneous setting and process. Am Miner 88:806–816

Karner JM, Sutton SR, Papike JJ, Shearer CK, Jones HH, Newville M (2006) Application of a new vanadium valence oxybarometer to basaltic glasses from the Earth, Moon and Mars. Am Miner 91:270–277

Kesson SE, Lindsley DH (1975) The effects of Al^{3+}, Cr^{3+}, and Ti^{3+} on the stability of armalcolite. In: Proc. Lunar Sci. Conf. 4th, pp 911–920

Kowalski PM, Wunder B, Jahn S (2013) Ab initio prediction of equilibrium boron isotope fractionation between minerals and aqueous fluids at high P and T. Geochim Cosmochim Acta 101:285–301

Krawczynski MJ, Sutton, Grove TL, Newville M (2009) Titanium oxidation state and coordination in the lunar high-titanium glass source mantle. In: Proceedings of the 40th lunar and planetary science conference, n. 2164

Krawczynski MJ, Sutton SR, Barr JA, Grove TL (2010) Titanium valence in lunar ultramafic glasses and olivine-diogenites. In: Proceedings of the 41st lunar and planetary science conference, n. 1825

Kress V, Ghiorso M, Lastuka C (2004) Microsoft EXCEL spreadsheet-based program for calculating equilibrium gas speciation in the COHS-Cl-F system. Comput Geosci 30(3):211–214

Leitzke FP, Fonseca ROC, Michely LT, Sprung P, Münker C, Heuser A, Blanchard H (2016) The effect of titanium on the partitioning behavior of high-field strength elements between silicates, oxides and lunar basaltic melts with applications to the origin of mare basalts. Chem Geol 440:219–238

Lombard P, Boizet B, Ollier N, Jouin A, Yoshikawa A (2009) Spectroscopic studies of Ti^{3+} ions speciation inside $MgAl_2O_4$ spinels. J Cryst Growth 311:899–903

Longhi J (1987) Liquidus equilibria and solid solution in the system $CaAl_2Si_2O_8$–Mg_2SiO_4–$CaSiO_3$–SiO_2 at low pressure. Am J Sci 287:265–331

Ma C, Rossman GR (2009a) Tistarite, Ti_2O_3, a new refractory mineral from the Allende meteorite. Am Miner 94:841–844
Ma C, Rossman GR (2009b) Grossmanite, $CaTi^{3+}AlSiO_6$, a new pyroxene from the Allende meteorite. Am Miner 94:1491–1494
Mallmann G, O'Neill HSC (2009) The crystal/melt partitioning of V during mantle melting as a function of oxygen fugacity compared with some other elements (Al, P, Ca, Sc, Ti, Cr, Fe, Ga, Y, Zr and Nb). J Petrol 50:1765–1794
Mallmann G, Wykes J, Berry A, O'Neill HSTC, Cline CJ, Turner S, Rushmer TA (2016) In situ XANES of U and Th in silicate liquids at high pressure and temperature. In: American geophysical union, fall general assembly 2016, abstract id. MR13A-2418
Marvin UB, Walker D (1978) Implications of a titanium-rich glass clod at Oceanus Procellarum. Am Miner 63:924–929
Meyer C (2012) Lunar sample compendium. http://curator.jsc.nasa.gov/lunar/compendium.cfm. Accessed 15 Dec 2017
Millet MA, Dauphas N (2014) Ultra-precise titanium stable isotope measurements by double-spike high resolution MC-ICP-MS. J Anal At Spectrom (29):1444–1458
Millet MA, Dauphas N, Greber ND, Burton KW, Dale CW, Debret B, Macpherson CG, Nowell GM, Williams HM (2016) Titanium stable isotope investigation of magmatic processes on the Earth and Moon. Earth Planet Sci Lett 449:197–205
Mollo S, Blundy JD, Iezzi G, Scarlato P, Langone A (2013) The partitioning of trace elements between clinopyroxene and trachybasaltic melt during rapid cooling and crystal growth. Contrib Miner Petrol 166:1633–1654
Moore CB, Lewis CF, Cripe J, Delles FM, Kelley WR (1972) Total carbon, nitrogen, and sulfur in Apollo 14 lunar samples. Proc Third Lunar Sci Conf Geochim et Cosmochim Acta 2(Suppl. 3):2059–2068
Myers J, Eugster HP (1983) The system Fe–Si–O: oxygen buffer calibrations to 1500 K. Contrib. Mineral Pet 82:75–90
Nazzareni S, Moli G, Skogby H, Dal Negro A (2004) Crystal chemistry of Ti^{3+}–Ti^{4+} bearing synthetic diopsides. Eur J Mineral 16:443–449
Ni H, Keppler H (2013) Carbon in silicate melts. Rev Mineral Geochem 75:251–287
Nicholis M, Rutherford MJ (2009) Graphite oxidation in the Apollo 17 orange glass 797 magma: implications for the generation of a lunar volcanic gas phase. Geochim Cosmochim Acta 73(19):5905–5917
O'Hara MJ, Niu Y (2015) Obvious problems in lunar petrogenesis and new perspectives. Geol Soc Am Spec Pap 514:339–366
O'Neill HSTC, Eggins SM (2002) The effect of melt composition on trace element partitioning: an experimental investigation of the activity coefficients of FeO, NiO, CoO, MoO_2 and MoO_3 in silicate melts. Chem Geol 186:151–181
O'Neill HSC, Berry AJ, Eggins SM (2008) The solubility and oxidation state of tungsten in silicate melts: implications for the comparative chemistry of W and Mo in planetary differentiation processes. Chem Geol 255:346–359
Papike JJ, Parker JM, Shearer CK (2005) Comparative planetary mineralogy: valence state partitioning of Cr, Fe, Ti, and V among crystallographic sites in olivine, pyroxene, and spinel from planetary basalts. Am Miner 90:277–290
Papike JJ, Simon SB, Burger PV, Bell AS, Shearer CK, Karner JM (2016) Chromium, vanadium, and titanium valence systematics in Solar System pyroxene as a recorder of oxygen fugacity, planetary provenance, and processes. Am Mineral 101:907–918
Pavicevic M, Ramdohr P, Goresy E, A (1972) Electron microprobe investigations of the oxidation states of Fe and Ti in ilmenite in Apollo 11, Apollo 12, and Apollo 14 crystalline rocks. In: Proceedings of the third lunar science conference, pp 295–303
Prewitt TC, Shannon RD, White WB (1972) Synthesis of a pyroxene containing trivalent titanium. Contrib Miner Petrol 35:77–82
Quartieri S, Antonioli G, Artioli G, Lottici PP (1993) XANES study of titanium coordination in natural diopsidic pyroxenes. Eur J Mineral 5:1101–1109
Ravel B, Newville M (2005) ATHENA, ARTEMIS, HEPHAESTUS: data analysis for X-ray absorption spectroscopy using IFEFFIT. J Synchrotron Radiat 12:537–541
Righter K, Sutton S, Danielson L, Pando K, Schmidt G, Yang H, Berthet S, Newville M, Choi Y, Downs RT, Malavergne V (2011) The effect of fO_2 on the partitioning and valence of V and Cr in garnet/melt pairs and the relation to terrestrial mantle V and Cr content. Am Miner 96:1278–1290
Righter K, Danielson LR, Pando KM, Shofner GA, Sutton SR, Newville M, Lee CT (2016) Valence and metal/silicate partitioning of Mo: implications for conditions of Earth accretion and core formation. Earth Planet Sci Lett 437:89–100
Ringwood AE, Kesson SE (1976) A dynamic model for mare basalt petrogenesis. Proc 7th Lunar Planet Sci Conf 7:1697–1722
Rushmer T, Dixon NA, Clark SM (2015) High pressure, down under: the first Australian high-pressure synchrotron facility for geoscience research. Aust J Earth Sci 62:181–188
Sato M (1976) Oxygen fugacity and other thermochemical parameters of Apollo 17 high-Ti basalts and their implications on the reduction mechanism. In: Proceedings of the 7th lunar science conference, pp 1323–1344
Sato M, Hickling NL, McLane JE (1973) Oxygen fugacity values of Apollo 12, 14 and 15 lunar samples and reduced state of lunar magmas. In: Proceedings of the Fourth Lunar Science Conference, Supplement 4, Geochimica et Cosmochimica Acta, vol 1, pp 1061–1079
Schauble EA, Mheut M, Hill PS (2009) Combining metal stable isotope fractionation theory with experiments. Elements 5:369–374
Schreiber HD (1986) Redox processes in glass-forming melts. J Non Cryst Solids 84:129–141
Schreiber HD, Balasz GB (1982) Vanadium as an oxygen geobarometer in basaltic magmas: the further development of a geochemical electromotive force series in silicate melts. In: Lunar and Planetary Science Conference, XIII, pp 692–693
Sepp B, Kunzmann T (2001) The stability of clinopyroxene in the system CaO-MgO-SiO_2-TiO_2 (CMST). Am Mineral 86:265–270
Simon SB, Sutton SR (2017) Valence of Ti, V, and Cr in Apollo 14 aluminous basalts 14053 and 14072. Meteorit Planet Sci 52:2051–2066
Simon SB, Sutton SR (2018) Valences of Ti, Cr, and V in Apollo 17 high-Ti and very low-Ti basalts and implications for their formation. Meteorit Planet Sci. https://doi.org/10.1111/maps.13123
Simon SB, Sutton SR, Grossmann L (2007) Valence of titanium and vanadium in pyroxene in refractory inclusion interiors and rims. Geochim Cosmochim Acta 71:3098–3118
Simon SB, Sutton SR, Grossmann L (2014) Valence of Ti in lunar igneous rocks: the first direct measurements. In: Proceedings of the 45th lunar and planetary science conference, p 1063
Simon SB, Sutton SR, Grossmann L (2016) The valence and coordination of titanium in ordinary and enstatite chondrites. Geochim Cosmochim Acta 189:377–390
Simons B, Woermann E (1978) Iron Titanium oxides in equilibrium with metallic iron. Contrib Miner Petrol 66:81–89
Stanin FT, Taylor L (1980) Armalcolite—an oxygen fugacity indicator. In: Lunar and planetary science conference, 11th, Houston TX, March 17–21, 1980, proceedings (A82-22251 09–91), vol 1. Pergamon, New York, pp 117–124
Sung CM, Abu-Eid RM, Burns RG (1974) A search for trivalent titanium in Apollo 17 pyroxenes. In: Proceedings V lunar and planetary science conference, pp 758–760
Sutton SR, Jones KW, Gordon B, Rivers ML, Bajt S, Smith JV (1993) Reduced chromium in olivine grains from lunar basalt 15555:

X-ray absorption near edge structure (XANES). Geochim Cosmochim Acta 57:461–468

Sutton SR, Goodrich CA, Wirick S (2017) Titanium, vanadium and chromium valences in silicates of ungrouped achondrite NWA 7325 and ureilite Y-791538 record highly-reduced origins. Geochim Cosmochim Acta 204:313–330

Taylor LA, Patachen A, Mayne RG, Taylor DH (2004) The most reduced rock from the moon, Apollo 14 basalt 14053: its unique features and their origin. Am Miner 89:1617–1624

Troullier N, Martins JL (1991) Efficient pseudopotentials for plane-wave calculations. Phys Rev B 43:1993–2006

Urey HC (1947) The thermodynamic properties of isotopic substances. J Chem Soc 1947:562–581

Warren PH, Taylor GJ (2014) The moon. In: Treatise on geochemistry, 2nd edn, Elsevier, pp 213–250

Waychunas GA (1987) Synchrotron radiation XANES spectroscopy of Ti in minerals: effects of Ti bonding distances, Ti valence, and site geometry on absorption edge structure. Am Miner 72:89–101

Wechsler BA, Prewitt CT, Papike JJ (1975) Structure and chemistry of lunar and synthetic armalcolite. Lunar Sci VI:860–862

Wilke M, Partzsch GM, Welter E, Farges F (2007) Redox reaction in silicate melts monitored by "static" in-situ Fe K-edge XANES up to 1180 °C. AIP Conf Proc 882:293. https://doi.org/10.1063/1.2644505

Wong J, Lytle FW, Messmer RP, Maylotte DH (1984) K-edge absorption spectra of selected vanadium compounds. Phys Rev B 30:5596–5609

Wunder B, Meixner A, Romer RL, Jahn S (2011) Li-isotope fractionation between silicates and fluids: pressure dependence and influence of the bonding environment. Eur J Mineral 23:333–342

Zhang J, Dauphas N, Davis AM, Leya I, Fedkin A (2012) The proto-Earth as a significant source of lunar material. Nat Geosci 5:251–255